Volume 2
Number 2
April 2026
Pages 299-710

EES Batteries

rsc.li/EESBatteries

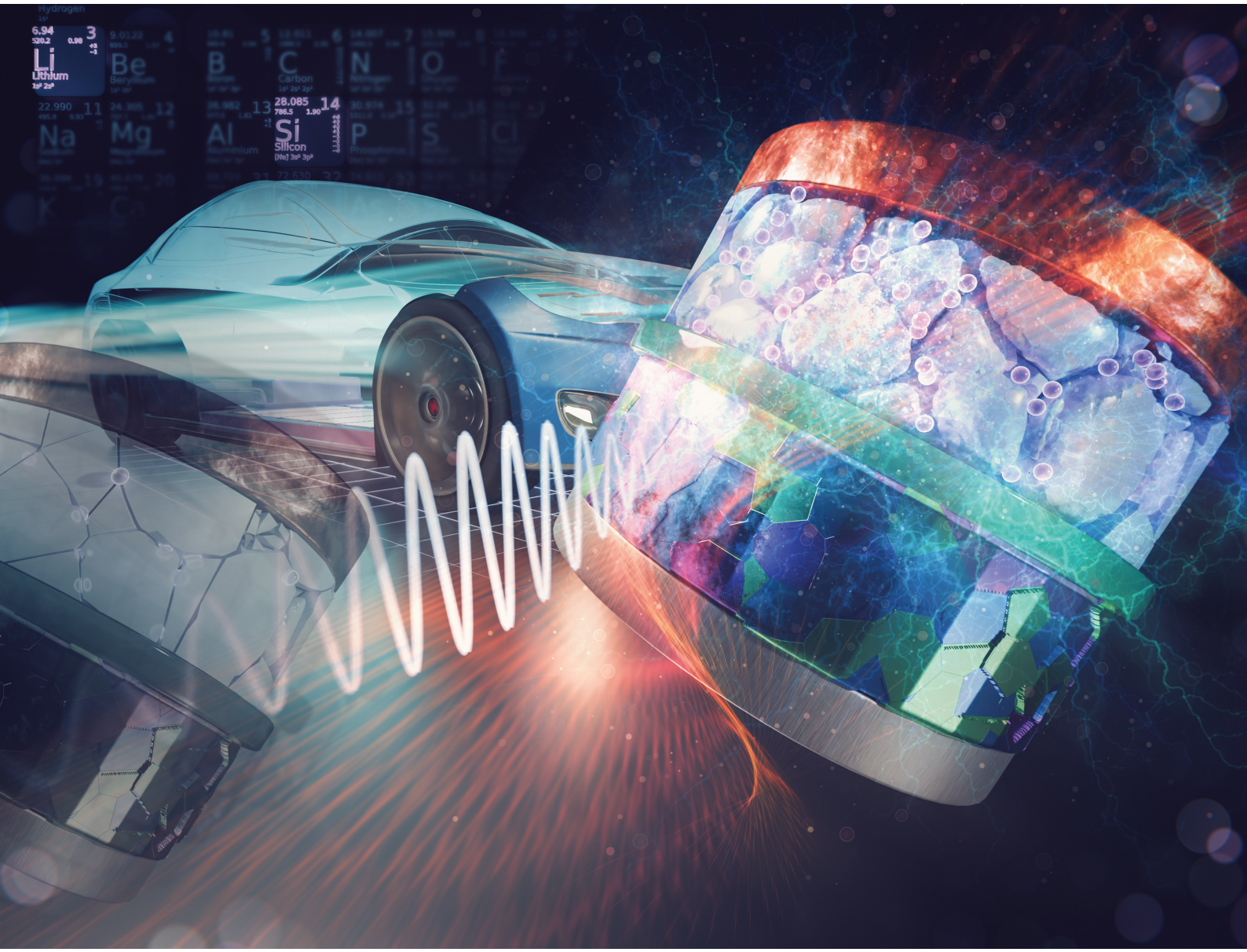

ISSN 3033-4071

ROYAL SOCIETY OF CHEMISTRY

PAPER

Michael Häusler, Roland Brunner *et al.*
Bridging particle-scale lithiation mechanisms and macroscopic performance in high-energy density Si anodes *via* time-resolved full 3D visualisation

EES Batteries

PAPER

View Article Online
View Journal | View Issue

Check for updates

Cite this: *EES Batteries*, 2026, **2**, 446

Bridging particle-scale lithiation mechanisms and macroscopic performance in high-energy density Si anodes *via* time-resolved full 3D visualisation

Michael Häusler, [a] Rahulkumar J. Sinojiya, [a] Olga Stamati,[b] Julie Villanova,[c] Christoph Stangl,[d] Stefan Koller[d] and Roland Brunner *[a]

Anodes with high silicon (Si) content paired with nickel–manganese–cobalt (NMC) cathodes enable interesting prospects for Li-ion batteries well beyond the state of the art. However, when Si alloys with lithium (Li), it undergoes significant volume changes, raising the critical question of how exactly the electrode and individual particles respond to the lithiation dynamics and thus impact the battery performance. Here, we provide enhanced insights into the chemo-mechanical processes for cells with an 89 wt% Si anode paired with an NMC cathode. Electrode-scale deformation is linked with particle-scale mechanics by incorporating correlative multiscale 3D *in situ* investigations. Indeed, the combination of a sophisticated *in situ* cell setup with synchrotron X-ray computed nano-tomography together with AI-driven segmentation and 4D strain mapping allows us to detect pronounced spatial deformation and strain heterogeneities from the electrode to the single particle level. We observe complex lithiation behaviours beyond the core–shell mechanism, anisotropic strain evolution and mechanically distinct transformation modes across hundreds of particles. These 4D multiscale observations demonstrate that the failure risk in electrodes with high silicon content is determined primarily by localized stress accumulation and microstructural conditions rather than by volume expansion alone, underscoring the need for a mechanistic understanding of chemo-mechanical degradation in Si-based anodes.

Received 30th January 2026,
Accepted 3rd February 2026

DOI: 10.1039/d6eb00026f

rsc.li/EESBatteries

Open Access Article. Published on 26 February 2026. Downloaded on 5/23/2026 9:12:27 AM.
This article is licensed under a Creative Commons Attribution 3.0 Unported Licence.

Broader context

The transition to a low-carbon economy and the reduction of transport-related emissions require lithium-ion batteries (LIBs) that combine high energy density with long-term stability. Paring nickel-manganese-cobalt cathodes (NMC) with silicon-rich anodes is widely seen as a promising way to exceed the performance limits of conventional graphite-based systems. However, the alloying of silicon with lithium leads to extreme volume changes that generate complex chemo-mechanical interactions across multiple length scales. The resulting stress build-up and microstructural damage ultimately drive performance degradation. A mechanistic understanding of these coupled processes remains a central bottleneck for next-generation batteries. In this work, we investigate a full cell configuration comprising an 89 wt% silicon anode paired with an NMC cathode. By combining in situ synchrotron-based X-ray nano-tomography with AI-assisted segmentation and 4D strain mapping, we directly correlate electrode-scale deformation with particle-scale mechanics during the lithiation of the anode. This correlative multiscale approach reveals pronounced spatial heterogeneities in deformation and strain, as well as complex lithiation pathways beyond the classical core-shell paradigm across hundreds of individual particles. Our results demonstrate that degradation in high-silicon electrodes is primarily determined by localised stress concentrations and microstructural constraints rather than by volume expansion alone. Establishing this mechanistic link between lithiation dynamics, strain localisation and failure risk provides a framework for the rational design of durable, high-energy-density lithium-ion batteries required for large-scale electrification.

Introduction

The electrification of transport is fundamental to the global effort to decarbonize energy systems and mitigate climate change. Lithium-ion batteries (LIBs) support this transition, not only powering electric vehicles, but also enabling grid-scale storage and facilitating the integration of intermittent renewable energy sources. Widespread adoption across sectors depends on overcoming key performance bottlenecks, particularly in energy density, charging speed and cycle life, while ensuring long-term economic and environmental sustainability.[1–3]

The success of LIBs arises from their high energy density, long cycle life and high efficiency. In automotive applications, industry targets exceed 250 Wh kg^{-1} energy density, >2C

[a]*Materials Center Leoben Forschung GmbH, 8700 Leoben, Austria.*
E-mail: roland.brunner@mcl.at
[b]*Univ. Grenoble Alpes, CNRS, Grenoble INP, 3SR, 38000 Grenoble, France*
[c]*ESRF-The European Synchrotron, ID16B, 38000 Grenoble, France*
[d]*Varta Innovation GmbH, 8020 Graz, Austria*

© 2026 The Author(s). Published by the Royal Society of Chemistry

Open Access Article. Published on 26 February 2026. Downloaded on 5/23/2026 9:12:27 AM. This article is licensed under a Creative Commons Attribution 3.0 Unported Licence.

charge rates and >1000 cycles.[4] These demands have driven the development of high-performance cathode materials, particularly those based on nickel, manganese and cobalt (NMC), which enable higher capacity and voltage windows.[5] However, the graphite anode, currently dominant in commercial LIBs, is limited by a theoretical capacity of ~372 mAh g^{-1} (ref. 6) and suffers from limitations under high charging rates due to lithium plating.[4] As a result, the anode becomes the limiting component and pairing it with high-capacity NMC cathodes cannot fully unlock the desired performance for next-generation applications.

To address this mismatch, alloy-type anodes have emerged as promising alternatives.[7,8] These materials react with lithium to form alloys, allowing much higher capacities than intercalation-based systems. Among them, silicon stands out due to its high theoretical specific capacity (~4200 mAh g^{-1} for $Li_{22}Si_5$), low working potential, natural abundance and compatibility with existing manufacturing infrastructure.[1,8–11] In combination with NMC cathodes, silicon anodes offer a path towards high-energy-density LIBs.[7,12,13] However, the key challenge remains the large volume changes silicon undergoes during (de)lithiation,[11,14] leading to capacity fading and decreased cycle life.[11,13,15–18] Despite extensive engineering strategies to mitigate these effects,[8,9,19–22] the widespread commercial implementation of ultra-high silicon content anodes remains challenging. Correlated investigations of lithiation dynamics, stress evolution and degradation at both the electrode and particle levels are important for advancing Si-rich anodes toward practical full-cell architectures, including pairings with NMC cathodes.

It is widely reported that lithiation of crystalline silicon proceeds *via* a two-phase core–shell mechanism.[23–26] A moving amorphization front converts crystalline Si (c-Si) into amorphous Li_xSi, leading to radial expansion and internal stress accumulation. Much of this understanding stems from *in situ* transmission electron microscopy (TEM) studies on idealized systems that use statistically non-representative amounts of Si particles, neglect the electrode microstructure, including porosity and carbon binder domain (CBD), and are conducted under vacuum.[27,28] While TEM enables high spatial resolution, it is inherently two-dimensional, requires invasive sample preparation, is restricted to a small field of view and is limited in its ability to capture interparticle interactions, matrix effects, or collective behaviour within intact electrodes. As such, these observations provide limited insight into real-world battery configurations.[8,9,19,20,27,28]

Recently, *in situ* three-dimensional imaging techniques have gained momentum in battery research, offering new opportunities to bridge the gap between model systems and realistic architectures.[29–31] In this context, synchrotron-based X-ray computed tomography (nano-SXCT) enables three-dimensional imaging at the nanoscale from two-dimensional projections collected over a 360° rotation. Prior studies utilizing nano-SXCT have revealed macroscale phenomena in battery cells such as electrode swelling, crack formation and delamination during cycling.[32–38] However, most *in situ* nano-SXCT experiments operate at voxel sizes above 0.2 μm,[32,34–39] insufficient to resolve sub-micron features of individual silicon particles, typically 500 nm–5 μm in diameter, in embedded electrodes. Consequently, particle-scale phenomena, such as heterogeneous lithiation, stress localization and interparticle interactions, remain unresolved in three-dimensions, despite their central role in degradation cascades that affect entire electrodes. Moreover, while Li metal half-cell configurations are invaluable for mechanistic *in situ* investigations, they do not fully reproduce key electrochemical and mechanical constraints of full cells. Full-cell configurations can therefore provide complementary insights when it comes to translating particle-level chemo-mechanics to practical architectures.[36–40] Yet, sub-micron, *in situ* 3D imaging of silicon particles embedded within an electrode microstructure would allow direct tracking of critical early-stage microstructure degradation processes and local lithiation behaviour on different length scales that have so far remained hidden. A recent study combining *operando* optical microscopy and synchrotron X-ray computed tomography with digital volume correlation revealed heterogeneous lithiation dynamics and strain evolution in graphite/μ-Si composite electrodes at the electrode scale, highlighting that Si cycling stability critically depends on intraparticle nanoscale porosity, whereas mechanical degradation is driven largely by the expansion of the carbon-binder domain (CBD).[41] Yet, full correlative *in situ* chemo-mechanical studies on Si|NMC cells that track behaviour from the electrode scale down to individual particles at sub-micron resolution unravelling lithiation pathways, stress concentrator and fracture nucleation in 3D over time remain scarce.

Herein, we apply *in situ* nano-SXCT to investigate the lithiation behaviour and mechanical response of a high 89 wt% Si anode paired with an 811NMC cathode in three dimensions from the electrode to particle level in a correlated manner. Our custom-designed electrochemical cell applies a controlled stack pressure to ensure electrical contact and mechanical relevance during cycling. This enables time-resolved 3D tracking of the electrode, Si particle's adjacent microstructure and the individual silicon particle dynamics with sufficient resolution and contrast beyond the state of the art. The possibility to capture 4D *in situ* data down to the nanoscale in combination with semantic image segmentation and local digital volume correlation (DVC)-based analysis allows the collection of high spatio-temporal resolved full-field displacement and strain maps. We not only analyse the lithiation behaviour of the electrode but also enhance the perception of the chemo-mechanical process by studying diverse local lithiation behaviours, anisotropic strain evolution and mechanically distinct transformation modes from hundreds of particles distributed within the electrode to individual ones. Rather than a uniform core–shell transformation, many particles develop internal, complex network-like lithiated pathways. The in-depth correlative multi-scale tomographic analysis suggests that Si lithiation is thus intrinsically heterogeneous, governed by global and local features such as the particle size distribution, particle location within the electrode and surrounding microstructure, state of charge and also by processing-induced damage, the electrode

Open Access Article. Published on 26 February 2026. Downloaded on 5/23/2026 9:12:27 AM.
This article is licensed under a Creative Commons Attribution 3.0 Unported Licence.

architecture as well as cell configuration, respectively. These observations point to factors to consider in silicon-anode development such as defect screening, particle-size optimization and architecture engineering. Furthermore, the multi-scale correlative *in situ* nano-SXCT-based framework generalizes to different materials and cycling conditions, combining nanoscale resolution with mechanical analysis to support the rational design of next-generation electrodes.

Results and discussion

In situ measurement setup and electrochemical cell behaviour

We build a cell setup, allowing *in situ* synchrotron X-ray computed nano-tomography acquisition to investigate electrochemically induced transformations of the electrode and Si particles during lithiation and delithiation with high resolution and contrast; see Fig. 1. The cell geometry is scaled down to fit the requirements of nanoscale tomography and to ensure the detection of sub-micron object sizes, while maintaining the design and material elements of high energy density, commercially relevant LIBs; see Fig. 1a. The measurements are performed at the ID16B beamline[42] of the European Synchrotron Radiation Facility (ESRF), Grenoble, France.

The anode consists of a slurry-cast layer containing 89 wt% micron-sized crystalline silicon particles connected by a polyacrylic acid (PAA)-based binder, carbon black and carbon nanotubes, calendered to a final thickness of ~21 μm. Graphite is deliberately excluded from the anode to isolate the chemo-mechanical responses of silicon,[1,7] which is often

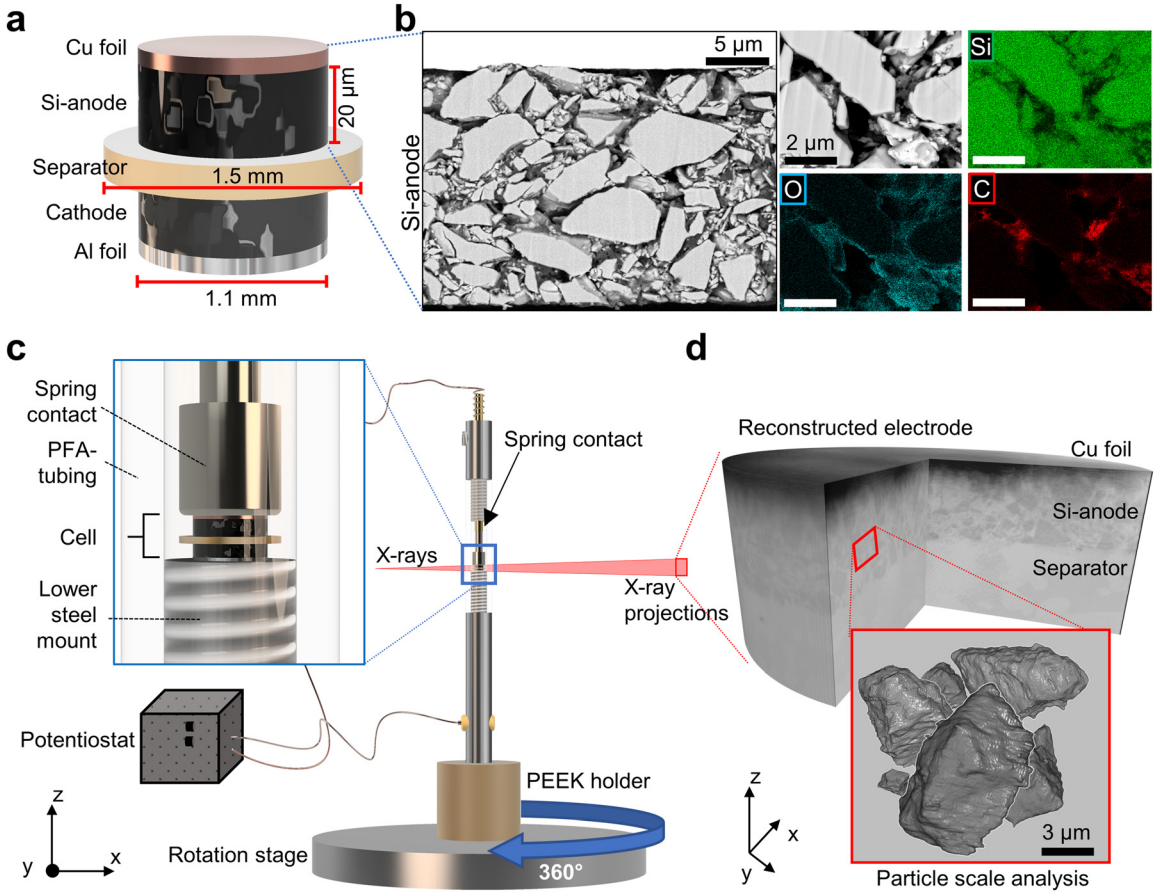

Fig. 1 Nano-SXCT setup and custom *in situ* cell. (a) Schematic of the layered Li-ion cell utilized for the *in situ* nano-SXCT experiment at ESRF ID16B. The cell consists of a ~20 μm thick, silicon-based anode and an NMC cathode with a 1.1 mm diameter, coated onto a copper and aluminium current collector, respectively. In between the electrodes, an electrolyte-soaked separator with a 1.5 mm diameter is placed. (b) Backscattered electron (BSE) FESEM cross-section of the pristine anode, showing the copper current collector at the top. The right-hand panels display the EDS maps of silicon (Si), oxygen (O) and carbon (C), from a magnified region, highlighting silicon particles and the carbon binder domain (CBD). The anode is graphite-free. (c) *In situ* cell assembly: the cell is inserted into a PFA tube (inner/outer ∅: 1.6/3.2 mm). The tube is then closed on both ends with stainless-steel screw mounts. A spring contact is adjusted to apply a predefined external pressure and to ensure stable electrical contact. The assembly is mounted onto a PEEK support at the rotation stage. Electrical connection from the potentiostat to the cell is established *via* a banana plug at the lower mount and by wrapping a 0.8 mm copper wire around the top of the spring contact, respectively. During tomography, the X-ray beam passes perpendicular to the rotation axis in the *xy*-direction. (d) Reconstructed nano-SXCT volume (field of view: 102.4 × 102.4 × 102.4 μm^3; voxel size: 50 nm). The dark top layer is the copper foil, beneath that is the Si anode and the bright layer corresponds to the separator. The measurement resolves the particle scale morphology suitable for quantitative analysis.

© 2026 The Author(s). Published by the Royal Society of Chemistry

Open Access Article. Published on 26 February 2026. Downloaded on 5/23/2026 9:12:27 AM. This article is licensed under a Creative Commons Attribution 3.0 Unported Licence.

obscured in composite systems. The prepared Si-based anode is stacked with a polypropylene separator and paired with an NMC811 cathode, forming a full-cell configuration, enabling *in situ* nano-tomography under full-cell-relevant electrochemical and mechanical boundary conditions, which complement Li-metal half-cell studies.[36–40] To avoid fully exploiting the large Si capacity, the anode is operated under cathode-limited conditions (Materials and methods section). This cathode-limited balancing is chosen to ensure a stable cycle during time-resolved nano-tomography and to quantify chemical–mechanical heterogeneity and early-stage damage precursors.

Fig. 1b illustrates the structural and chemical composition of the pristine anode utilizing backscattered electron (BSE) field emission scanning electron microscopy (FESEM) imaging and energy-dispersive X-ray spectroscopy (EDS). The correlated images reveal the distribution of silicon particles embedded in the carbon-binder domain (CBD).

The prepared anode|separator|cathode-stack is integrated into the custom-designed *in situ* cell and mounted on the rotation stage at ID16B as shown in Fig. 1c. A key feature of the cell design is a spring-loaded upper contact which applies a constant compressive load of about 0.2–0.4 MPa, replicating real-world conditions.[43] Furthermore, the spring is able to accommodate changes in the electrode stack thickness during cycling, maintaining uniform interfacial contact and stable electrochemical performance throughout lithiation and delithiation. While some previous *in situ* X-ray studies have used defined-pressure systems to replicate realistic mechanical environments, these approaches have typically been limited to larger-scale setups and have not been adapted for X-ray nano-tomography at microscale dimensions.[37,39,40] Other studies, in contrast, relied on hand-assembled or loosely packed capillary cells without controlled pressure,[37,38,44,45] often resulting in inconsistent compression and limited reproducibility. Further details on cell assembly, electrochemical testing and the systematic pre-testing of prototype cells to verify the electrochemical response, including voltage profiles and sealing integrity, are provided in the Materials and methods section and SI Notes S1–S3.

Fig. 1d shows a reconstructed nano-SXCT volume with a field of view of 102.4 × 102.4 × 102.4 μm^3 and a voxel size of 50 nm. The dark top layer is the Cu current collector, the Si anode lies beneath and the bright layer corresponds to the separator. The dataset resolves particle-scale morphology suitable for quantitative analysis.

3D electrode and individual Si particle morphology evolution during Li insertion

Fig. 2a illustrates the reconstructed aligned nano-SXCT volumes of the electrode across different states of lithiation, from the uncycled, pristine state at T0 to the lithiated condition at T6, corresponding to approximately 85% state of charge (SoC) of the full cell as defined by the cathode-limited capacity. The *in situ* cell design introduced in Fig. 1 enables not only monitoring of electrode-scale morphological evolution but also correlative tracking of individual silicon particles during lithiation in three dimensions (Fig. 2b), exceeding the capabilities of previous studies.[37,38,46] The effective spatial resolution of approximately 300 nm (see further details in Fig. S8) enables sub-micron feature resolution at the particle scale while preserving the statistically relevant electrode-level context. The copper current collector remains unchanged throughout the experiment and serves as a reliable internal reference for further analysis.

During lithiation, the anode thickness increases in an approximately linear manner, as observed qualitatively in Fig. 2a and SI Video S1 and quantified in Fig. 2c. In detail, the mean electrode thickness increases from 20.7 ± 0.7 μm at T0 to 25.8 ± 1.8 μm at T3 (50% SoC) and reaches 30.0 ± 2.1 μm at T6, corresponding to a cumulative average thickness increase of about 44%. Despite the substantial overall expansion, no macroscopic cracking through the entire electrode thickness, as reported in previous studies,[37,38] is observed at any point during lithiation. Stepwise analysis reveals incremental increases of about 5 to 7% between T1 and T2, T3 and T4, as well as T4 and T5, while a noticeable steeper increase occurs between T2 and T3. This transition coincides with the onset of the 4.3 V constant voltage stage (Fig. 2d), indicating a change in the electrochemical reaction regime. This behaviour is characteristic of the first lithiation of Si-rich anodes, where extensive and partly unstable SEI formation promotes continued electrolyte reduction and side reactions at a constant potential. Consequently, a fraction of the CV current is consumed by interphase growth rather than by active lithiation.[47] Furthermore, the specific nano-SXCT cell geometry (~1 mm electrode diameter) and the *in situ* SXCT protocol require intermittent pauses for tomographic imaging, which can lead to electrochemical relaxation and charge redistribution within the electrode. Upon resumption of constant voltage operation, such redistribution effects can temporarily increase the measured current without causing proportional additional electrode expansion. More details regarding the cell performance and reproducibility are provided in SI Note S2 and Fig. S4, while measurement and electrochemical protocols are described in the Materials and methods section and SI Note S3.

For quantitative particle-level analysis, the detectability of silicon relies on phase-contrast imaging, which is sensitive to variations in the real part of the refractive index (δ).[48] To assess the evolution of phase contrast during lithiation, grey-scale intensity profiles are extracted both across the Si particle interface and within the particle core, as illustrated in Fig. 2e and f, with corresponding cross-sectional slices indicating the profile locations. The particle centre of mass is fixed to allow direct comparison between time steps. At T0, the pristine crystalline Si particle is embedded within the CBD infiltrated by the electrolyte (E). In this pristine state, crystalline Si exhibits strong phase contrast relative to the surrounding CBD + E, resulting in a well-defined particle interface (interface T0), which is marked by a pronounced decrease in greyscale intensity (Fig. 2e).

© 2026 The Author(s). Published by the Royal Society of Chemistry

Open Access Article. Published on 26 February 2026. Downloaded on 5/23/2026 9:12:27 AM.
This article is licensed under a Creative Commons Attribution 3.0 Unported Licence.

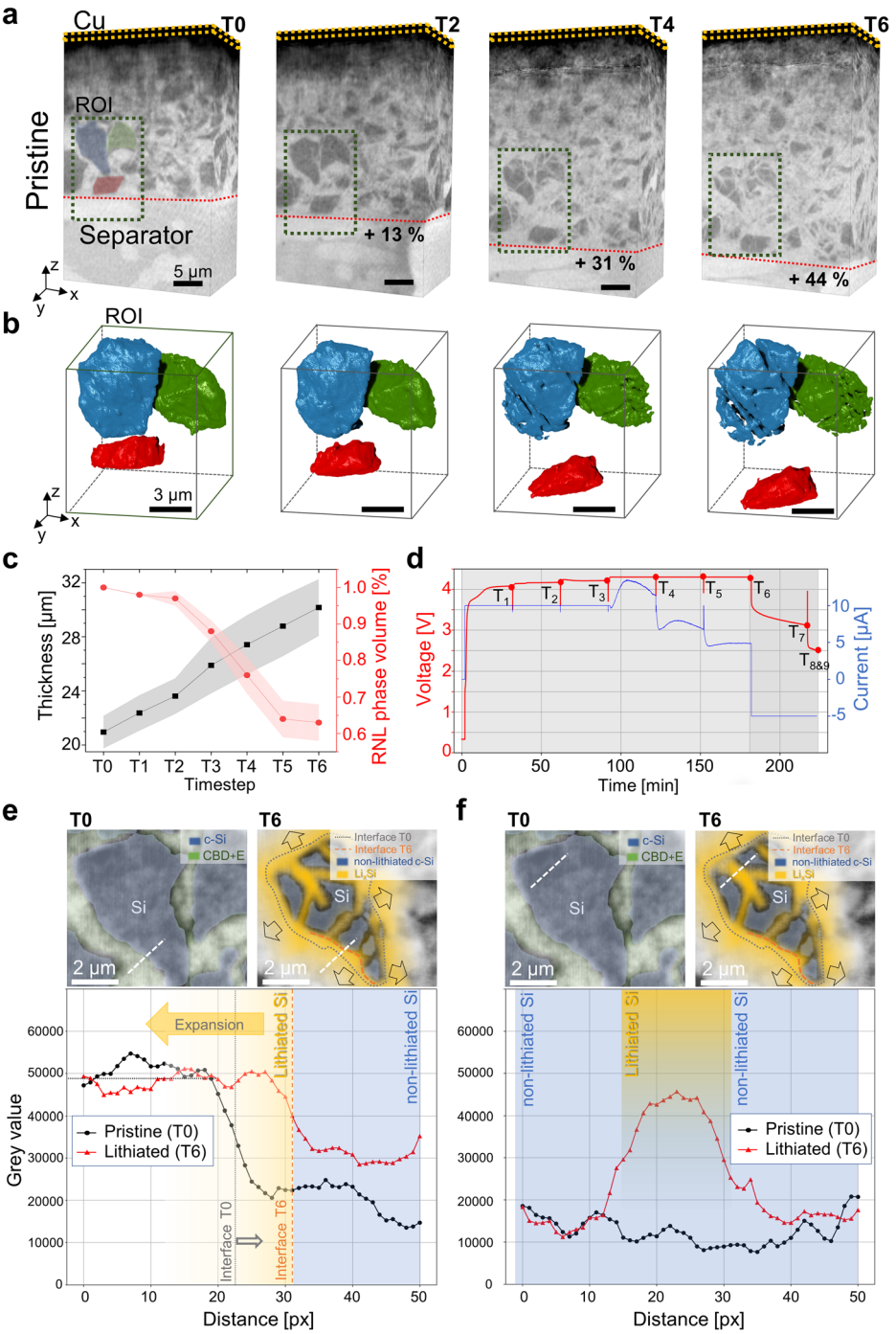

Fig. 2 Morphological evolution and phase-contrast-driven segmentation of the non-lithiated silicon phase upon charging. (a) Representative nano-SXCT reconstructions of the anode from timesteps T0 (pristine) to T6 (cell: ~85% SoC) with the Cu current collector (orange dotted line) and indicated porous separator. At the pristine state (T0) the Si particles and CBD + E are indicated by dark and light grey colours, respectively. Electrode expansion is highlighted by the dashed red line. The ROI to study the evolution at the particle level is indicated by a green dotted box. Representative particles are highlighted in red, green and blue colours. The scalebar refers to 5 µm. (b) The ROI to track representative particles in red, green and blue, respectively, during charging using semantic segmentation. The segmentation only shows non-lithiated silicon. Scalebars refer to 3 µm. (c) Axial average anode thickness and relative non-lithiated (RNL) phase volume from the Si particles distributed in the electrode from T0 to T6. (d) Cell voltage profile during the charge–discharge cycle, with tomographic acquisition points T0–T9 indicated. Charging is performed at constant current (C/3) to 4.3 V, followed by a constant–voltage hold. At T6 the cell reaches ~85% SoC. T7–T9 are acquired during and after partial discharge at C/5 to 2.5 V. (e and f) Nano-SXCT cross-sections of a representative particle at T0 and T6, together with greyscale intensity profiles extracted along the dashed white lines to assess lithiation. At T0, pristine crystalline Si (blue) and CBD + E (green) are observed. At T6, the particle consists of non-lithiated Si (blue), exhibiting a similar greyscale value to pristine Si, and lithiated Si (orange), which shows greyscale values comparable to CBD + E at T0. The orange dashed line marks the interface between lithiated and non-lithiated Si at T6. The original extent of the pristine particle at T0 is indicated by the grey dotted outline, highlighting particle expansion beyond the initial interface upon lithiation.

© 2026 The Author(s). Published by the Royal Society of Chemistry

Open Access Article. Published on 26 February 2026. Downloaded on 5/23/2026 9:12:27 AM. This article is licensed under a Creative Commons Attribution 3.0 Unported Licence.

Fig. 2f illustrates greyscale profiles drawn entirely within the particle's core. At T0, the profile is flat across the considered range, indicating a homogeneous crystalline phase with uniform phase contrast. At T6, the profile initially exhibits a similar greyscale value to that of pristine Si, indicating the presence of remaining non-lithiated crystalline regions within the particle. Further along the profile, a significant increase in greyscale intensity is observed, followed by a subsequent decrease, reflecting the transition from non-lithiated to lithiated silicon within the particle interior. As lithiation progresses, the refractive index of silicon changes,[49] causing lithiated silicon to exhibit a phase contrast increasingly similar to that of the surrounding CBD + E; see the corresponding cross section image. Consequently, only the non-lithiated portion of the silicon particle remains clearly distinguishable in the reconstructed volumes.

To quantify the evolution of the non-lithiated silicon phase throughout the electrode, a convolutional neural network (CNN)-based semantic segmentation model is applied to all time steps, see Fig. 2b and c. Further details regarding the deep learning model are given in the Materials and methods section and SI Note S4. The time series in Fig. 2b reveals an apparent increase in inter-particle spacing and a progressive reduction in the segmented particle volume during lithiation. Fig. 2c shows that the relative non-lithiated (RNL) Si phase volume decreases gradually up to T2 and more abruptly between T2 and T3, consistent with both the electrode thickness evolution and the electrochemical profile in Fig. 2d. For instance, the blue-labelled particle in Fig. 2b shows a segmented volume decrease from 119 μm^3 at T0 to 80 μm^3 at T6, indicating that approximately 33% of the crystalline core has become lithiated by T6.

Importantly, this apparent particle shrinkage does not correspond to a physical contraction of the silicon particles. Instead, it reflects a progressive loss of phase contrast as crystalline silicon transforms into lithiated silicon, which becomes increasingly indistinguishable from the surrounding CBD + E in phase-contrast SXCT. This interpretation is further supported by overlaying the pristine particle contour obtained at T0 onto the cross-section at T6 (Fig. 2e), which reveals a locally dependent retreat of the visible particle boundary relative to the original interface. At T6, the greyscale profile exhibits a reduced slope and a shift of approximately 8 pixels toward the particle centre compared to T0, marking the transition from non-lithiated to lithiated silicon and emphasizing the difficulty of defining the true particle boundary during lithiation.

Capturing the global deformation of the electrode

We quantify the chemo-mechanical response by applying a local digital volume correlation (local-DVC) based analysis[50] to the time-resolved synchrotron tomograms, extracting full-field displacements and strains. Specifically, this approach features a mechanical perspective of the underlying morphological changes, bridging the gap between visual observations, mechanical response and electrochemical behaviour. We register all timesteps to the pristine state of the electrode at timestep T0 using cubic correlation windows placed on a regular 3D grid. A 50% overlap between adjacent windows is used to resolve displacement gradients at the particle scale while maintaining robust convergence of the iterative correlation. Displacement vectors at window centres provide the local strain tensor. See the schematics in Fig. 3a and b for the grid and principle. Details with respect to the DVC model are presented in the Materials and methods section and SI Note S5.

Fig. 3c shows the evolution of axial strain maps for the vertical cross-sections from the electrode. The underlying dynamics is exemplarily illustrated by timesteps T2, T4, and T6. This indicates that the deformation is dominated by expansion along the thickness in the axial direction. The effective visualized axial strain ranges from compressive to tensile, illustrated in blue and red, respectively. First localized tensile zones appear at T2, establishing a separator-to-collector gradient in the very first lithiation step. These zones intensify and connect as lithiation proceeds significantly as indicated in timestep T4 and peak at T6 on the separator side. A partial relaxation during delithiation is observed at T8.

More detailed strain analysis of the electrode is performed by mapping the temporal evolution of the extracted mean volumetric strain across the full anode as well as bottom and top electrode parts, associated with the separator and current-collector sides, respectively; see Fig. 3d. The mean volumetric strain of the full electrode increases by about 6% upon initial lithiation at T1 and then progressively builds up throughout the constant current and constant voltage charging, reaching roughly 44% at T6. The measured electrode expansion (see also the analysis in Fig. 2a) is consistent with previous reports.[17,41,51] All these values remain well below the often-cited theoretical volumetric expansion of ~300% for fully lithiated pure Si.[11,17,52]

In full-cell configurations, actual expansion is significantly constrained by factors such as limited lithiation depth, anode to cathode balance, mechanical confinement, porosity and the influence of surrounding matrix materials. This discrepancy highlights the limitations of earlier studies, which often employed idealized systems that neglect electrode-scale mechanical particle interactions. Therefore, a critical perspective is required when interpreting both theoretical expansion values and data derived from simplified experimental setups.

During lithium extraction from T6 to T8, the electrode exhibits partial strain recovery, but a residual volumetric strain of ~32% persists; see the dark shaded area in Fig. 3d. The presence of an irreversible strain component suggests underlying permanent microstructural changes, such as solid electrolyte interphase (SEI) growth or plastic deformation.[53]

Indeed, a deeper understanding regarding the asymmetry of the strain distribution in the electrode is gained by analysing the upper region adjacent to the current collector and lower region near the separator of the electrode, separately. As shown in Fig. 3d, strain differences are small at early stages of lithiation, see timestep T2, but diverge with the state of charge. By T6 the separator-side region averages about 50% volumetric strain, while the current-collector side averages about 34%.

© 2026 The Author(s). Published by the Royal Society of Chemistry

Open Access Article. Published on 26 February 2026. Downloaded on 5/23/2026 9:12:27 AM.
This article is licensed under a Creative Commons Attribution 3.0 Unported Licence.

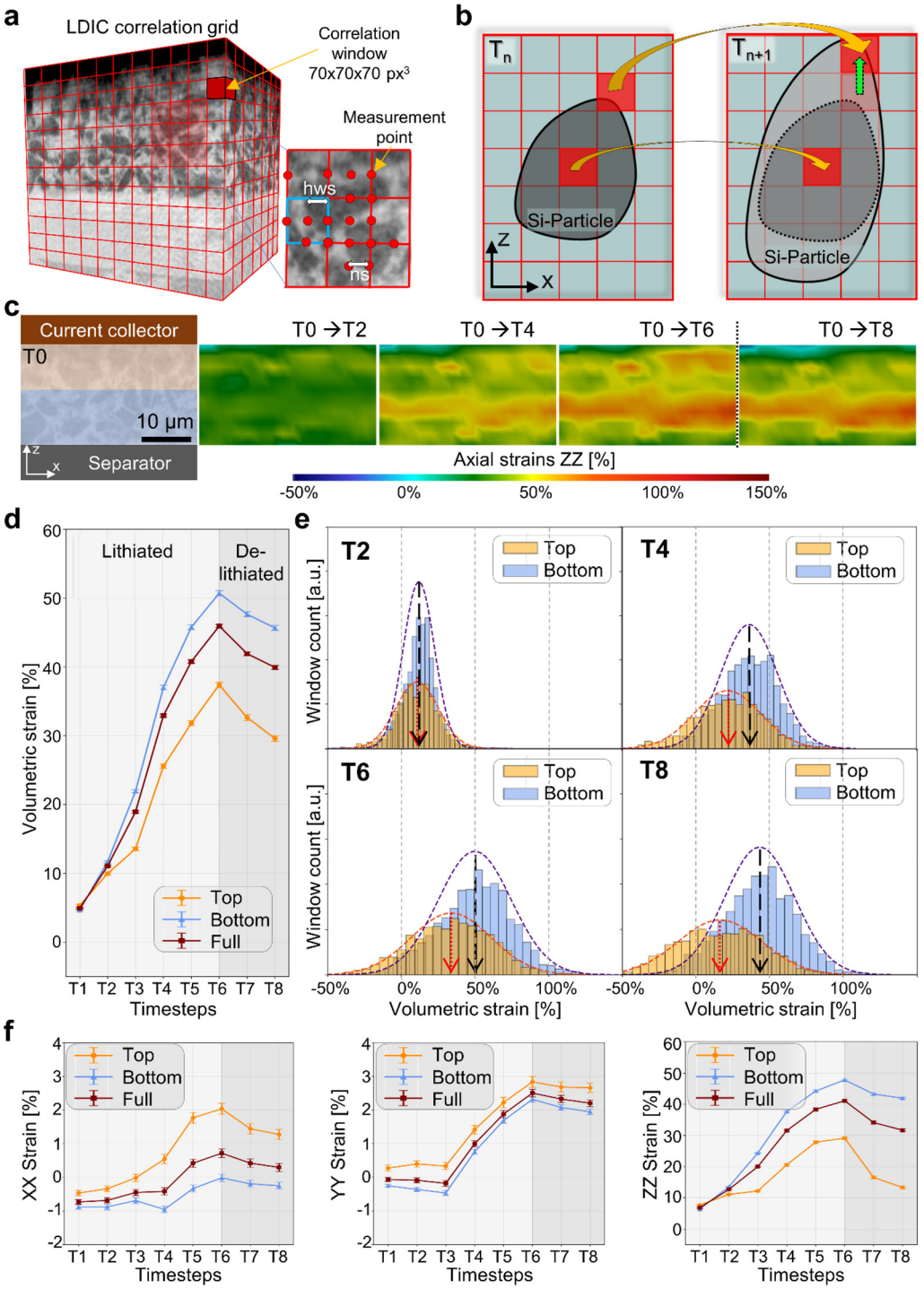

Fig. 3 Electrode-scale evolution of volumetric and axial strain. (a) Local digital volume correlation (local-DVC) grid on a representative anode sub-volume (40 × 40 × 40 µm^3) at T0. A node spacing (ns) of 35 voxels and a half window size (hws) of 35 voxels give overlapping 70^3-voxel correlation windows (red cube). (b) DVC principle: a regular grid of correlation windows is tracked between a reference volume (T*n*) and a deformed volume (T*n* + 1), yielding local displacement vectors at window centres (illustrated by a green arrow). From the displacement field, local strain tensors are computed. The schematic of a deforming Si particle illustrates this approach. (c) A nano-SXCT vertical cross-section (T0) indicating the divided current-collector side (orange) and separator side (blue). Right: corresponding axial strain maps at T2, T4, T6 and T8 referenced to T0. Effective axial strain is mapped from compressive (blue, −50%) to tensile (red, +150%). The scale bar corresponds to 10 µm. (d) Evolution of volumetric strain is shown for the current collector (orange) and separator (blue) side, as well as for the entire electrode (red), revealing spatial heterogeneity. (e) Extracted histograms indicate the local volumetric strain distributions in the current-collector (Top) and separator (Bottom) electrode side at T2, T4, T6 and T8. Maxima are highlighted by arrows. Progressive broadening and skewing of the strain distributions indicate increasing heterogeneity and asymmetry. (f) Temporal evolution of the axial strain components (*XX*, *YY*, and *ZZ*) over the entire anode (red). Light grey and dark grey backgrounds indicate timepoints corresponding to lithiation and delithiation, respectively. Orange and blue lines represent the strain in the top and bottom side of the electrode, respectively.

© 2026 The Author(s). Published by the Royal Society of Chemistry

Open Access Article. Published on 26 February 2026. Downloaded on 5/23/2026 9:12:27 AM. This article is licensed under a Creative Commons Attribution 3.0 Unported Licence.

Furthermore, we quantified the emergence of strain heterogeneity by plotting the histograms of volumetric strain for the two regions at T2, T4, T6, and T8; see Fig. 3e. At timestep T2 both distributions are narrow and centred likewise, consistent with a uniform expansion. However, as lithiation progresses, the distributions broaden significantly, reflecting increased spatial heterogeneity. By T6 the separator-side distribution at the bottom of the electrode shows strain values exceeding 100% in some areas, while the current-collector side at the top includes areas with compressive strains down to −50%.

In Fig. 3f the temporal evolution of the mean axial strain components *XX*, *YY* and *ZZ* over the entire anode is further studied to understand the dominant mechanical loading direction. The results show that, at the electrode level, the measurable net deformation tends strongly towards the thickness (z), while the strain components in the plane remain comparatively low. The in-plane strain components ε_{xx} and ε_{yy} remain below 3% throughout, whereas the majority of the observable volumetric change manifests as axial strain ε_{zz}. This observation aligns with the macroscopic electrode swelling shown in Fig. 2a and reflects the inherent mechanical anisotropy of the cell, governed by stack pressure and boundary conditions. It also is in accordance with the particle movement illustrated in Fig. 2b. The independent particle tracking based on segmentation (see details in Fig. S9) supports further the presented strain analysis. While lateral particle displacements in the *xy*-plane are minimal, axial displacements vary markedly with the position within the electrode. Particles near the current collector shift by ∼2 μm, while those near the separator move up to ∼11 μm, corresponding to local swelling of nearly 60%. It is important to note that these displacements reflect a collective deformation at the electrode level rather than the free expansion of individual particles that are mechanically connected to the surrounding matrix.

The observed axial strain gradient reflects the combined effect of boundary conditions, transport asymmetry and collective mechanical confinement within the electrode. Mechanical constraints are imposed asymmetrically along the electrode thickness. Expansion in the direction of the current collector is severely constrained, while deformation in the direction of the fibrous separator is less restricted. In contrast, expansion in the plane is restricted overall by the laterally continuous electrode, which extends far beyond the field of view shown. The analysed volume (∼100 μm lateral expansion) is embedded in an electrode disc with a diameter of ∼1.1 mm, so that lateral expansion would require a coordinated displacement of the surrounding material outside the field of view, which would make in-plane stretching unfavourable. As a result, volume changes caused by lithiation manifest themselves preferentially as axial deformation at the electrode level, even though there is no explicit external in-plane pressure. This mechanically biased deformation couples with lithium transport from the separator side, leading to preferential lithiation, SEI formation and strain accumulation near the separator interface.[54]

Three-dimensional strain evolution in the particle vicinity during Li insertion and extraction

The local mechanics is further analysed in three dimensions around individual particles distributed in the electrode upon charging and discharging, to uncover the chemo-mechanical process at the particle level. As depicted in Fig. S10, the lithiated anode exhibits modest local thickness variations across the field of view, indicating non-uniform lithiation kinetics and local stress concentration sites within the electrode. To trace the evolution of the particle vicinity in three-dimensions, we isolate 15 × 15 × 15 μm^3 sub-volumes centred on an exemplary silicon particle located in the electrode under investigation; see Fig. 4a. All timesteps are spatially aligned based on the centre of mass of this central particle at each respective timestep. The approach fixes a particle-centric reference frame that removes global rigid body motion and electrode-scale expansion from the local analysis. Subsequently, volumetric strain fields are computed between successive timesteps from T0 → T2, T2 → T4, T4 → T6 and T6 → T8; see Fig. 4b. In this frame, the central particle exhibits near-zero apparent strain by design, while surrounding windows capture the relative deformation of the neighbouring microstructure, described by other particles, CBD and pore network. The evaluated successive three-dimensional strain maps show progressive inhomogeneous accumulation of tensile strain in the neighbourhood of the centred Si particle during lithiation, reaching a maximum at timestep T6. Displacement vectors indicate expansion toward locally compliant pores in the vicinity of the particle. After partial delithiation at T8, strain magnitudes decrease relative to T6 and return to levels between those observed at T4 and T5, which exhibit a similar SoC. This trend is consistent with alloy driven expansion of Si and partial reversibility upon Li extraction which generates mechanical stress in confined architectures.[11,14,26,55] Additionally, solid electrolyte interphase growth may also contribute to the observed deformation.[56–59]

Next the impact of the surrounding microstructure on the particle-resolved strain distribution in different planes is assessed in more detail. Hence, orthogonal slices through the three-dimensional microstructure at timestep T6 relative to T0 are presented in Fig. 4c. The volumetric strain distribution projected on the microstructure reveals for different planes that regions containing many smaller sized particles (sp-Si), embedded in CBD, exhibit elevated strain, whereas narrow gaps confined between closely packed large particles (lp-Si) show comparatively low strain. Furthermore, high local porosity near particles accommodates expansion by pore collapse and thereby helps to relieve strain. Hence, an inhomogeneous strain field in the vicinity of the particle conditioned by the microstructure results, also suggesting significant impact on the lithiation at the particle's interface; see Fig. 2e and f. Post-mortem FESEM cross-sections at the electrode level (see Fig. S11) support these observations, revealing microstructural precursors for strain localization such as binder-rich zones, porosity variations and a highly inhomogeneous Si particle

Open Access Article. Published on 26 February 2026. Downloaded on 5/23/2026 9:12:27 AM.
This article is licensed under a Creative Commons Attribution 3.0 Unported Licence.

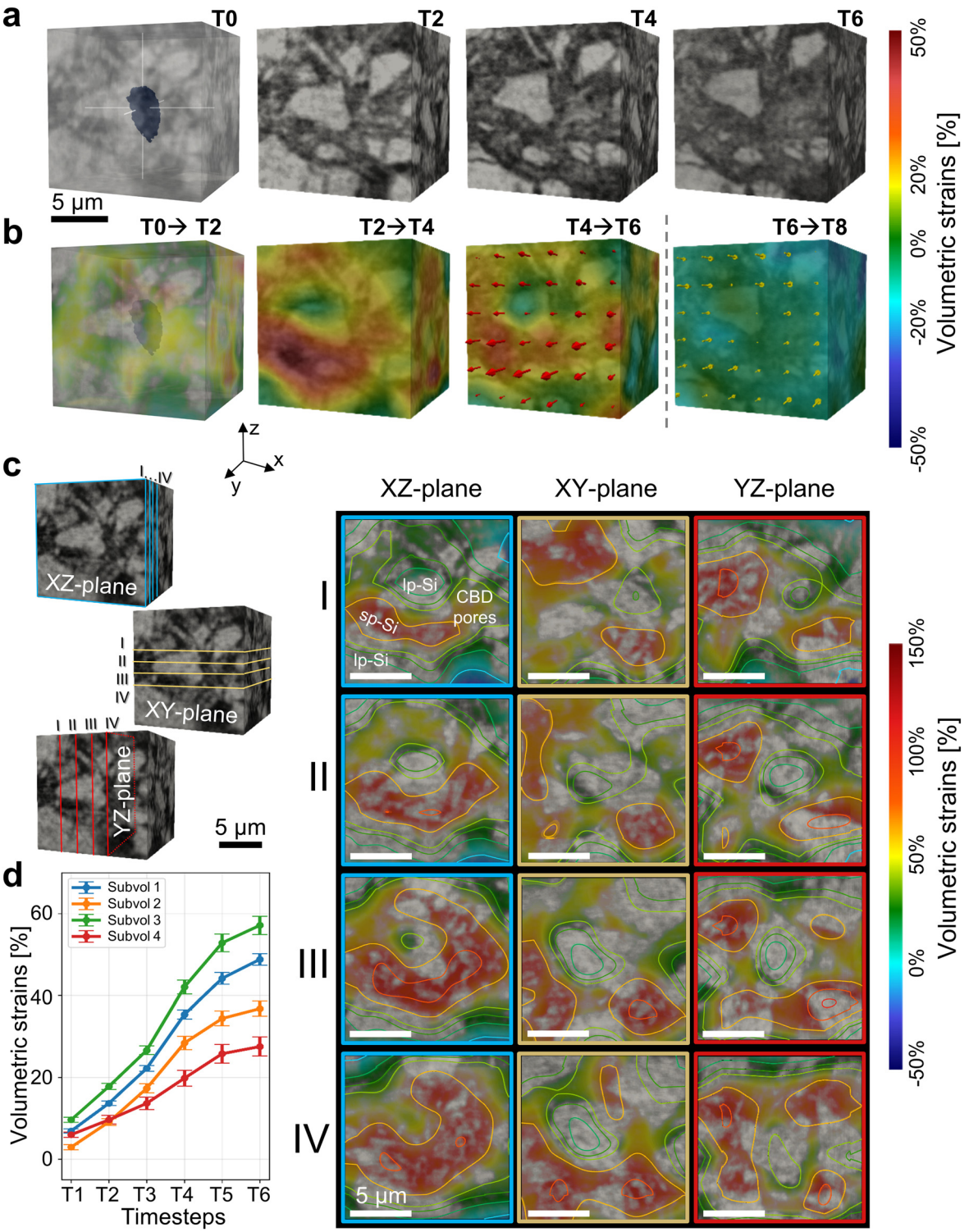

Fig. 4 Volumetric strain analysis at the particle level. (a) Nano-SXCT reconstructions of 15 × 15 × 15 µm^3 sub-volumes at T0, T2, T4 and T6. The T0 volume is rendered semi-transparent to highlight the central particle to which all timesteps are registered. (b) Incremental three-dimensional volumetric-strain maps, each referenced to a preceding step, *e.g.* T0 → T2, whereas T0 → T2 illustrates exemplarily a transparent 3D representation to highlight the central particle. The corresponding morphology is overlaid to facilitate interpretation of local strain changes during (de)lithiation. The strain colormap spans compressive −50% (blue) to tensile +50% (red). Furthermore, displacement vectors to indicate local expansion directions are shown for T4 → T6 and T6 → T8. (c) Orthogonal views of volumetric strain at T6 relative to T0, overlaid on the T0 microstructure. Slices are extracted along the planes indicated in the 3D renderings (blue, *XZ*; yellow, *XY*; and red, *YZ*). Contours mark equal-strain levels. Four equally spaced slices are depicted along each orientation to visualize in-plane variations. The strain colormap spans compressive −50% (blue) to tensile +50% (red). Small and large Si particles, indicated by sp-Si and lp-Si, respectively, are shown in light grey and CBD/pores in dark grey. Scale bars, 5 µm. (d) Temporal evolution of volumetric strain for four additional particle-centred volumes of interest.

© 2026 The Author(s). Published by the Royal Society of Chemistry

Open Access Article. Published on 26 February 2026. Downloaded on 5/23/2026 9:12:27 AM. This article is licensed under a Creative Commons Attribution 3.0 Unported Licence.

size distribution. Regions dominated by large Si particles show only a minor irreversible thickness increase, whereas areas rich in sub-micron particles exhibit greater residual thickening, consistent with enhanced SEI formation driven by their higher surface area.[60,61] Thus, the resulting depicted three-dimensional inhomogeneous strain in the particle vicinity affects the chemical reaction and further deepens the understanding of the underlying chemo-mechanical process. This observation is in line with prior findings[62–64] which have identified SEI constituents such as fluorine-rich layers and carbonate-based species, as well as residual Li_xSi phases that resist full delithiation, as contributing factors to irreversible expansion.

Pronounced strain heterogeneity within the electrode becomes even more evident when analysing multiple particle-centred volumes of interest (VOI); see Fig. 4d. The analysis provides important information concerning the initial chemo-mechanical process, which is indeed highly relevant for observations made at longer cycling.[17,18] It reveals that location-dependent strain heterogeneity emerges already at the first cycle of the cell within the anode microstructure. Between T1 and T2 the mean volumetric strain increases similarly across VOIs, but the strain evolution diverges strongly as lithiation progresses, consistent with the trends in Fig. 2 and 3. At T6, some VOIs exhibit modest average volumetric strain of about 25%, whereas others reach 60% (*e.g.*, subvolume 4 and 3, respectively), with local peaks larger than 150% at inter-particle contacts and within constricted pore regions. See also Fig. S12 for further details.

Furthermore, local heterogeneities can also be triggered by temporary low-density features that occur within the electrode, as shown in the tomographic time series in Fig. S13. An exemplary feature occurs between timesteps T1 and T2 and disappears again between T4 and T5. Due to the pronounced grey value contrast compared to that of silicon and the surrounding electrolyte CBD matrix, this feature could correspond either to a transient gas bubble, possibly caused by electrolyte decomposition or reactions with trace moisture,[65–67] or to a temporarily isolated cavity that is not wetted by the electrolyte due to local electrode or binder degradation. Regardless of their exact origin, the temporary occurrence of such low-density areas can lead to local concentration or relaxation of stresses, disrupt particle networks and contribute to mechanically induced heterogeneities, as confirmed by volumetric strain analysis.

Divergent particle-level responses revealed by residual analysis

The key challenge is to study spatially the mechanical response of individual silicon particles during lithium insertion and extraction. Macroscopic deformation patterns arise from particle-scale dynamics and, in turn, bias those dynamics through changing contact networks and local confinement. To further resolve the underlying structural transformations, we compute DVC residual fields between two representative states extracted from the underlying electrode. The DVC-measured deformation is applied to the initial volume, geometrically matching it with the later configuration, *e.g.* the T0-deformed-to-T6 timestep. By subtracting the deformed volume of the initial state from the later dataset, we isolate residuals within the particle that reflect local material changes beyond mere positional shifts, and allow us to draw conclusion about the underlying particle lithiation behaviour; see the Materials and methods section for further details.

Fig. 5a and b contrast two distinct particle responses in 3D from timestep T1 to T6 and at T8, upon (de)lithiation. The exemplar core–shell(cs)-like particle in Fig. 5a shows faint, surface-limited residuals at T3 that evolve into a more continuous shell by timestep T6, while the core remains largely unchanged, consistent with a surface-limited lithiation front and minimal internal restructuring at the accessible spatial resolution. The Si particle core appears morphologically stable, with no visible cracks or internal microstructural transformations; see in particular timestep T6 where the particle is visualized together with the emerging residuals. Here, surface localized residuals and subtle grey-value shifts indicate limited lithiation-induced changes at the particle's periphery.

In contrast, the non-cs particle in Fig. 5b exhibits residual pathways that traverse the particle in all three directions at timestep T3. By T6 these pathways broaden, new branches appear and features brighten, indicating increasing local transformation and a complex distributed, 3D network-type lithiation. After partial delithiation at T8 (70% SoC) several pathways fade or retract, indicating partial reversibility. The onset and amplification of these changes are consistent with the macroscopic electrode response described above and follow the voltage characteristic; see in particular Fig. 3 and 2d. Orthogonal tomographic slices extracted at timesteps T3 and T6 along the planes indicated in Fig. 5a and b (T3) further resolve these structural characteristics and their evolution for the cs- and non-cs particles in more detail; see Fig. 5c, d and SI Videos S2 and S3. Here, the observed network-type lithiation indicates the ⟨110⟩ direction as the most favourable for Li-insertion.[18] A schematic comparing the lithium insertion and extraction for the cs and non-cs mechanisms is further illustrated in Fig. S14.

Fig. S15 shows an additional example of such emerging network structures upon partial lithium extraction within the particle. The study includes cases where the network contrast nearly disappears. Together, these observations indicate that cs-like particles remain predominantly surface-limited over T0–T8, whereas non-cs particles undergo internal, network-mediated transformation.

These branched, lithiated domains, observed here three-dimensionally during the first electrochemical cycle, extend and contextualise the two-dimensional post-mortem observations reported by Häusler *et al.*[18] The work shows that cycle-induced amorphous bands, presumably initiated by dislocation formation and dislocation accumulation, can form within the crystalline Si structure and impact the lithiation dynamics significantly. A further study pursuing *ex situ* TEM studies[68] on partially lithiated micrometre-sized silicon par-

Open Access Article. Published on 26 February 2026. Downloaded on 5/23/2026 9:12:27 AM.
This article is licensed under a Creative Commons Attribution 3.0 Unported Licence.

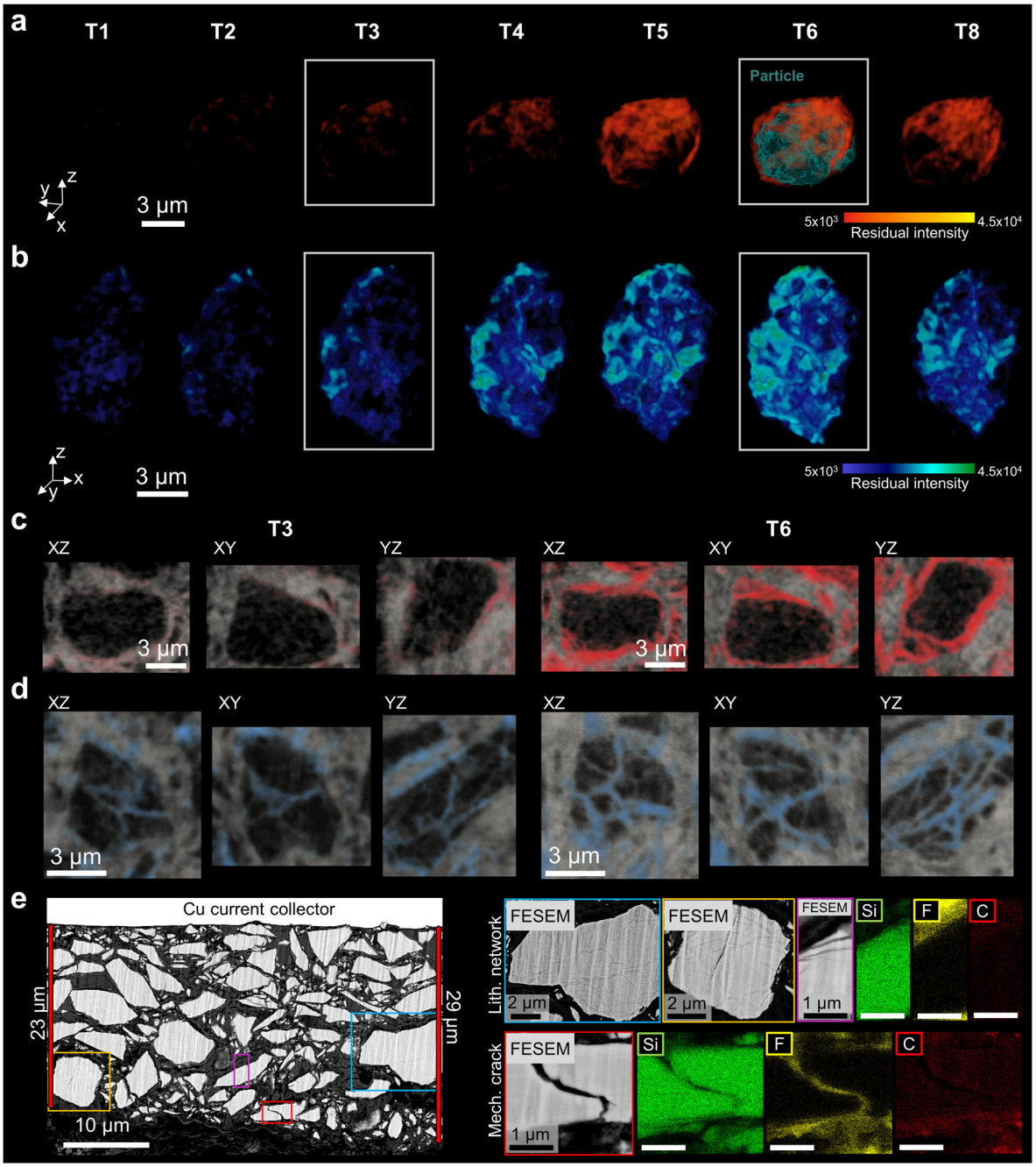

Fig. 5 Divergent particle-level responses to lithium insertion and extraction. (a and b) Time series for residual maps for a representative (a) core–shell (cs)-like and (b) non-cs-like (de)lithiation response. States T1, T2, T3, T4, T5, T6 and partially delithiated T8 illustrate the growth of residual features during lithiation and their partial regression upon lithium extraction within the Si particle. Higher residual intensity, in red and blue for cs- and non-cs-like, respectively, indicates regions with higher grey value changes upon (de)lithiation. For improved visibility of the cs-like residual structure, the particle contour is overlaid on the cs-like particle at T6. (c) Orthogonal tomographic slices in different planes exemplary at T3 and T6 of the cs-like particle shown in (a), with residual overlay (red contour). (d) Orthogonal slices at T3 and T6 for the non-cs particle shown in (b) with residual overlay (blue contour). Complex internal network emerges within an initially intact particle and intensify by T6 upon lithiation. Some features diminish after delithiation, consistent with a network-mediated transformation rather than a single advancing front. (e) Post-mortem FESEM of the cell with elemental EDS maps in the delithiated state (after T8) corroborates *in situ* observations. The anode cross-section exhibits pronounced thickness variations. Magnified regions (red,blue, orange and purple box) show network-like interiors in some particles with weak F and C signals (blue, orange, purple box), alongside particles displaying mechanical cracks *e.g.* (red box) with stronger F and C signal inside the crack.

© 2026 The Author(s). Published by the Royal Society of Chemistry

Open Access Article. Published on 26 February 2026. Downloaded on 5/23/2026 9:12:27 AM. This article is licensed under a Creative Commons Attribution 3.0 Unported Licence.

ticles supports the presence of such heterogeneous, non-radial lithiation pathways.

Here, we directly observe *in situ* during lithium insertion that these internal, network-like lithiation pathways are initiated at very early stages of the first cycle and may act as precursors to the amorphous regions reported[18,68] after prolonged cycling. The *in situ* four-dimensional measurements provide direct evidence that stress localization and heterogeneous lithiation emerge early within the particle core and likely govern the subsequent chemo-mechanical evolution and long-term performance of Si-based electrodes. These insights enable a deeper mechanistic understanding of particle- and electrode-level degradation in relation to electrochemical performance.

Fig. S16 also indicates particles already fractured before initial charging. Correlative analysis between particle and electrode-levels reveals that such pre-cracked particles are predominantly located near the electrode surface. Indeed, processing-induced damage during steps such as calendering might explain the performed observation. The presented post-mortem FESEM imaging of the delithiated electrode after one cycle in Fig. 5e corroborates the *in situ*-based nano-SXCT analysis. A couple of particles display faint, network-like domains. EDS analysis of these regions within the Si particle reveal neither fluorine presence nor silicon loss, arguing against electrolyte infiltration or the onset of dendrite formation. Furthermore, it excludes fracture as the origin, since it affiliates to a different behaviour from that observed for the crack; see Fig. 5e. Fig. S17 further indicates that these networks expand with cycling.

The presented approach allows correlative 3D investigations over different length scales, from the cell to single particle-level. The results indicate that the classical and common core–shell mechanism represents only one of the several lithiation possibilities and strongly depends on the chemo-mechanical response. The latter is modulated by local particle-specific factors such as the defect state, local microstructural environment and lithiation kinetics. Within the scanned volume, illustrated in Fig. S18, the systematically manual-based screening shows that about 10% of the particles follow a cs-like response in the first lithiation insertion. Most common behaviour involves rather the lithiation along complex networks within the particle. The in-depth correlative multiscale tomographic analysis suggests that Si lithiation is thus intrinsically heterogeneous, governed by global and local features like the particle size distribution, particle location within the electrode and surrounding microstructure, and state of charge and also by processing-induced damage, electrode architecture and cell configuration, respectively.

Conclusion

This work provides enhanced insights into the chemo-mechanical process linking electrode-scale deformation to particle-scale mechanics for cells with high silicon (Si) content and paired with nickel–manganese–cobalt (NMC) cathodes, by combining correlative multiscale 3D *in situ* characterization. The combination of a pressure-controlled *in situ* cell design with high-resolution synchrotron X-ray nano-tomography, AI-driven segmentation and 4D strain mapping enables the detection of pronounced spatial deformation and strain heterogeneities from the electrode scale down to individual Si particles.

The observed strain heterogeneity on different length scales has direct implications for industrial electrode design. Micron-sized crystalline silicon particles, including those sourced from industrial cutting waste, offer a scalable and cost-effective alternative to engineered nanostructures[22] or sophisticated coated architectures,[21] but their successful deployment hinges on mitigating mechanically driven degradation. Our findings highlight several design levers for optimizing not only micron-sized Si but also nano-porous and other advanced Si architectures.

At the particle level, most particles do not follow a simple core–shell lithiation pathway. Instead, internal complex network-like transformation routes emerge within the particle and partly regress on delithiation, underscoring that silicon lithiation is governed by spatially heterogeneous reaction fronts rather than a uniform radial progression.

First, it is paramount to minimise defects caused during manufacturing, as existing cracks that occurred during particle synthesis can act as fracture nucleation sites. The introduction of quality control protocols during the particle manufacturing phase to detect and exclude cracked particles prior to electrode production could therefore reduce mechanical failures. However, additional particle damage can occur during electrode formulation and processing steps, particularly during calendering, where high compressive stresses can cause cracks in otherwise intact particles. Such processing-induced defects cannot be removed afterwards and must instead be addressed through optimised electrode design and processing conditions. Surface engineering to guide SEI formation and regulate lithium flux[69] could influence how and where lithiation begins, potentially steering the transformation pathway away from high-strain configurations.

Second, the particle adjacent microstructure, including pores, particle size and size distribution, has a strong influence on both the extent and reversibility of lithiation-induced strain since larger particles show a different lithiation behaviour from smaller ones. A narrower particle size distribution and a controlled pore structure could promote more uniform strain absorption across the entire electrode, thereby reducing local stress concentrations.

Third, our results highlight that mechanical failure is often dictated not by total expansion but by localized strain accumulation at both particle and electrode scales. The presented correlative multiscale framework provides a basis for engineering electrode architectures that moderate lithiation gradients and redistribute stress more evenly. Likewise, adjusting charging protocols, such as employing adaptive current profiles,[70,71] may reduce the severity of transient strain during fast charging and extend electrode lifetime.

© 2026 The Author(s). Published by the Royal Society of Chemistry

Open Access Article. Published on 26 February 2026. Downloaded on 5/23/2026 9:12:27 AM. This article is licensed under a Creative Commons Attribution 3.0 Unported Licence.

Taken together, these results show that the failure risk in electrodes with high silicon content is determined more by local stress accumulation and microstructural conditions than by volume expansion alone, underscoring the need for correlative multiscale 3D approaches for rational electrode design.

The observed electrochemical–mechanical behaviour reflects the response of a high-silicon electrode under conditions compatible with high-resolution nano-SXCT in a full-cell configuration. While these conditions limit absolute silicon utilisation, they provide direct access to particle and electrode heterogeneity that is not accessible in conventional cell formats.

Extending the same correlative 4D imaging and strain mapping framework to higher silicon utilisation regimes represents an important future direction to further bridge nano-scale *in situ* insights with commercial operating conditions.

By integrating advanced quantitative multiscale imaging, AI-based morphological analysis and mechanically realistic operating conditions, this study provides not only deeper understanding but also a diagnostic and design framework for durable, high-capacity Si anodes. The approach is broadly applicable beyond liquid-electrolyte Li-ion systems, including solid-state batteries employing Si-based anodes.

Materials and methods

Material preparation

The silicon-based anode was composed of 89 wt% micron-sized silicon particles (median size: 3–7 μm; CLM 00001/Wacker Chemie AG), 9 wt% polyacrylic acid (PAA)-based binder (AQUACHARGE (water solution)/SUMITOMO SEIKA), 1.8 wt% carbon black (Super C65/IMERYS) and 0.2 wt% single-walled carbon nanotubes (Tuball BATT H_2O/OCSIAL). The electrode slurry was cast onto a copper foil and subsequently calendered, yielding electrodes with an areal loading of 3 mg cm^{-2} and a theoretical areal capacity of approximately 11 mAh cm^{-2}. However, to avoid fully utilizing the anode's capacity, its effective capacity was limited to ~3.5 mAh cm^{-2} by pairing it with a cathode of matching capacity. As the cathode, a nickel–manganese–cobalt-oxide (NMC811, 3.5 mAh cm^{-2}), consisting of 96.5 wt% NMC811, 1.5 wt% PVDF-based binder and 1 wt% carbon black, was employed. Circular electrodes with a diameter of 1.100 ± 0.001 mm were precisely cut utilising a 3D Micromac microPREP PRO femtosecond laser with a laser power of 35 mW to ensure a reproducible geometry (see SI Note S1 for further details).

Cell assembly

The prepared electrode discs (1.100 ± 0.001 mm) were precisely assembled into a custom-designed *in situ* electrochemical cell, based on the setup described here.[37] A non-woven polypropylene separator (1.5 mm diameter), soaked in 0.5 μL electrolyte composed of 1 M lithium hexafluorophosphate ($LiPF_6$) in fluoroethylene carbonate (FEC) and diethyl carbonate (DEC) (2 : 8 v/v) with 2 wt% vinylene carbonate (VC), was placed between the electrodes. The cell housing was constructed from perfluoroalkoxy alkane (PFA) tubing (inner diameter: 1.6 mm and outer diameter: 3.2 mm), which is compatible with synchrotron imaging chosen for its low X-ray attenuation, chemical resistance and mechanical robustness.

Threaded stainless steel mounts were screwed into both ends of the tubing to create a sealed enclosure. A central feature of the cell design is the ability to apply a precisely adjustable and fixed mechanical pressure to the electrode stack *via* a spring-loaded contact inserted through the upper steel mount. For the 1.1 mm diameter cell used in this study, the applied pressure could be tuned across a wide range – from 0.01 to 1.5 MPa. During experiments, the spring was fixed to apply a constant pressure of 0.2–0.4 MPa. This adjustability is essential for optimizing and standardizing contact between cell components while minimizing mechanical deformation of the active material. A stable and defined pressure ensures consistent electrochemical performance and reproducibility between cells and preserves the integrity of microstructural evolution during *in situ* imaging. To maintain an inert environment and prevent air ingress, all interfaces between the steel mounts, polymer housing and spring contact were sealed with lacquer. The entire cell assembly was performed inside an argon-filled glovebox.

The complete cell setup was further mounted on a polyetheretherketone (PEEK) cylindrical-shaped support to ensure mechanical stability and chemical compatibility during cycling and imaging on the sample rotation stage at ID16B. Finally, the electrodes were electrically connected to a potentiostat.[72] For the lower mount (see Fig. 1c) a banana plug was utilized. At the upper terminal, a copper wire was wrapped tightly around the spring contact and further secured with parafilm. Soldering was avoided to prevent any heat-induced damage. The flexibility of the yet secure electrical setup enables sample rotation about the *z*-axis for uninterrupted *in situ* monitoring without compromising electrochemical or mechanical cell integrity. Additional assembly details are provided in SI Note S2. Despite employing several measures to ensure high-quality electrode fabrication and assembly, such as femtosecond laser cutting to ensure flat, uniform edges and a parallel layer stack, the high mass and electron density of Cu introduce X-ray scattering artefacts in the phase images, resulting in localized image degradation and blurring near the current collector in the resulting 3D volumes. Consequently, these blurred regions are excluded from strain analysis.

Electrochemical charging and discharging protocol

Electrochemical cycling was performed *in situ* using an OrigaFlex OGF500 potentiostat during synchrotron X-ray computed nano-tomography (nano-SXCT) acquisition using a custom script-controlled protocol. The cell was first charged using a two-step constant current–constant voltage (CC–CV) strategy. In the constant current (CC) phase, the cell was charged at a rate of C/3 until either a voltage of 4.3 V was reached or a maximum time of 30 minutes elapsed. If the voltage limit was reached before timeout, the protocol transi-

 © 2026 The Author(s). Published by the Royal Society of Chemistry

Open Access Article. Published on 26 February 2026. Downloaded on 5/23/2026 9:12:27 AM. This article is licensed under a Creative Commons Attribution 3.0 Unported Licence.

tioned into the constant voltage phase. Otherwise, a tomographic scan was triggered. In the subsequent constant voltage (CV) phase, the voltage was held at 4.3 V. Again, if either the current dropped below a predefined threshold (C/10) or 30 minutes had passed, a scan was initiated and the loop continued. The charging sequence continued until either a defined number of scans (n = 6) had been reached or the current had sufficiently stabilized.

Following the final charging scan, the cell was discharged under constant current conditions at a rate of C/6 until the lower voltage cut-off of 2.5 V was reached. To determine noise induced from the SXCT scan, two final scans without additional discharge at timesteps T8 and T9 were acquired without intervening electrochemical activity; see Fig. S19.

To minimize artefacts arising from mechanical or thermal relaxation during tomography, the cell was temporarily switched to an open-circuit voltage (OCV) one minute prior to each scan. Once acquisition was complete, electrochemical cycling resumed automatically. Further experimental details and a detailed flowchart of the control logic, including all decision pathways and fail-safes, are provided in the SI Note S3.

Cell SoC values reported in the main text refer to full-cell SoC. By design this corresponds to ~1/3 anode capacity utilisation (Materials and methods: Material preparation), owing to cathode-limited cycling.

In situ X-ray nano-tomography measurement

In situ X-ray nano-tomography was performed at the beamline ID16B[42] of the European Synchrotron Radiation Facility (ESRF) in Grenoble, France, using holo-tomography.[73] The imaging was conducted with a monochromatic, conical X-ray beam at an energy of 29.6 keV and a flux of ~10^{12} photons per second. Phase-contrast information was acquired by collecting radiographs at four different propagation distances, enabling accurate phase retrieval. Each tomographic dataset comprised 2505 projections acquired over a 360° sample rotation around the axial direction (z-direction), with an exposure time of 20 ms per projection. In addition, 20 flat-field and 21 dark-field images were recorded per scan. Data were collected using a PCO Edge 4.2 CMOS camera (2048 × 2048 pixels) coupled with a 30 μm thick LSO scintillator. The total acquisition time per holo-tomography scan was approximately 10 minutes. The voxel size for *in situ* scans was 50 × 50 × 50 nm^3.

Data reconstruction and processing

The 3D reconstruction was performed with the open-source software PyNX[74] through a two-step approach. Firstly, an iterative phase retrieval step was applied using as an initial guess a Paganin-like approach with a complex refraction index ratio δ/β = 170. Subsequently, a filtered back-projection reconstruction was performed using the ESRF software Nabu.[75] Ring artefact reduction was applied post-reconstruction using an in-house developed correction algorithm. The final reconstructed volumes (102.4 × 102.4 × 102.4 μm^3) were measured with a voxel size of 50 × 50 × 50 nm^3 and were saved in a 16-bit unsigned integer format. To enhance image contrast and improve visualization, histogram equalization was applied in a final post-processing step. All time steps were spatially aligned in relation to the position of the rigid copper current collector on top of the anode.

Machine-learning image segmentation

To segment different material phases in the reconstructed tomography volumes, a deep learning-based approach was applied using an attention residual U-Net architecture[76] implemented with the Python Keras library. Two separate models were trained to account for structural changes over time: Model 1 for early timesteps (T0–T2) and Model 2 for later stages (T3–T8). Initial labels were generated using Ilastik[77] and 12 annotated slice images per model (before augmentation) were selected for training. Image sizes were 256 × 512 px, with Model 1 using 4 slices per timestep and Model 2 using 2 slices per timestep. Data augmentation was performed to expand the dataset threefold. Both models were trained for 150 epochs on an NVIDIA RTX A5000 GPU. Additional details are provided in the SI. The final 3D visualization of the segmented data was accomplished using Dragonfly 3D World, Version 2024.1.[78]

Calculation of spatial resolution

Spatial resolution was estimated by analysing greyscale intensity transitions at particle interfaces. This involved manually selecting particle edges and extracting orthogonal line profiles across them. At these interfaces, the greyscale intensity exhibits characteristic changes due to phase contrast. The resolution was quantified as the full width at half maximum (FWHM) of the derivative of the greyscale profile, which was approximated by a quadratic function, following a similar approach described in Häusler *et al.*[72]. A representative line profile is provided in Fig. S8.

Strain analysis

Quantitative 3D strain analysis was performed using the open-source Software for Practical Analysis of Materials (SPAM),[50] which implements a digital volume correlation (DVC) based framework to measure 3D displacement and strain fields from a pair of X-ray tomography images. The analysis workflow began with two global registration steps: an initial "eye registration" for coarse manual alignment, followed by an automatic "non-rigid registration" step that estimates a single linear and homogeneous deformation function (Φ) mapping the reference image volume 1 into image 2 accounting for affine transformations: translations, rotations, normal and shear strain. The correlation procedure is based on a gradient-based iterative algorithm that minimizes the difference between the two images, progressively correcting the latter by a trial deformation function. Convergence is evaluated when a stable solution is reached, based on $\delta\Phi$ of the deformation function increment between two successive iterations. Local strain measurements were computed using SPAM's Local Digital Image Correlation (LDIC) module. This approach subdivides the image volume into a regular 3D grid of points and

Open Access Article. Published on 26 February 2026. Downloaded on 5/23/2026 9:12:27 AM. This article is licensed under a Creative Commons Attribution 3.0 Unported Licence.

performs independent non-rigid correlations within local sub-volumes (correlation windows) centred on each point. Material deformations were tracked solving the above iterative algorithm for each sub-volume across successive timepoints. A pyramidal refinement approach was employed to improve correlation resolution, progressively reducing the node spacing (ns) from 100 to 70 and finally to 35 pixels. The half-window size (hws) was set equal to the node spacing at each refinement step, ensuring 50% overlap between adjacent correlation windows. A final window size of $3.5 \times 3.5 \times 3.5$ μm^3 (70^3 voxels) was selected as optimal, balancing spatial resolution and convergence robustness. Displacement noise in the measured Φ-fields was filtered by replacing non-converged nodes with values interpolated from their neighbouring eight nodes before further processing. This filtering process helps to decrease the errors within the convergence loop. To quantify cumulative deformation over multiple timesteps, sequential deformation fields (*e.g.*, T0 → T1, T1 → T2, T2 → T3) were combined to construct cumulative mappings (such as T0 → T3) based on a multiplicative composition of the incremental local deformation functions. Total strain tensor components were then derived from the spatial gradients of these accumulative displacement fields using SPAM's strain field calculation routine, which operates on the regularly gridded displacement data. See also SI S5.

The strain mapping approach was applied at two spatial scales to capture both localized deformation around individual particles and global strain gradients across the electrode:

– Local strain analysis (particle-centred frame): to investigate local strain behaviour in the immediate vicinity of individual particles, cubic sub-volumes of $15 \times 15 \times 15$ μm^3 or $15 \times 15 \times 10$ μm^3 were extracted, each centred on a selected silicon particle. For each timestep, the particle's centre of mass was calculated and the sub-volume was cropped accordingly to establish a fixed local reference frame. This approach effectively removes global electrode displacements, isolating the relative deformation within each particle's neighbourhood (see Fig. S20).

– Electrode-scale strain mapping (electrode-centred frame): for electrode-scale analysis, the full imaged volume of $102.4 \times 102.4 \times 102.4$ μm^3 was subdivided into larger $40 \times 40 \times 40$ μm^3 regions (see Fig. S20), enabling spatially resolved strain mapping across the entire electrode thickness.

While scattering artefacts caused by Cu locally affect image quality near the current collector (see Fig. 2a) the affected area accounts for only a small portion of the analysed volume. The displacement fields remain clearly visible in this area, and the DVC-based strain analysis relies on volumetric correlations rather than sharp interfaces. We argue that strain trends in this area should be interpreted with appropriate caution, but nevertheless remain robust at the electrode level.

Residual mapping of local structural deviations based on DVC analysis

To visualize local structural deviations, residual maps were generated based on the accumulative multiplicative deformation fields (Φ). For each subsequent timepoint (T1 through T8), Φ-fields were computed relative to the reference state T0. These Φ-fields were then used to deform the reference image, generating predicted synthetically deformed volumes for each timepoint (*e.g.*, T0-deformed-to-T6). Residual images were obtained by subtracting the deformed reference image (T0-deformed-to-T6) from the corresponding original image at that timepoint (T6). Subtraction was performed in ImageJ (Fiji),[79] followed by a Gaussian blur ($\sigma = 2$) to suppress high-frequency noise and an (abs)-function to normalise the residual values. Finally, based on the double-scan error intensities, a level of 5000 residual values was considered as measurement noise and removed from the fields, isolating high residual features indicating non-linear structural transformation, as shown in Fig. S19.

FESEM analysis

Cross-sectional preparation of the anodes was performed using a Hitachi IM4000+ ion milling system, which employs low-energy argon ions to create clean cross sections without introducing mechanical stress to the sample. Field-emission scanning electron microscopy (FESEM) was conducted on a ZEISS GeminiSEM 450 at an acceleration voltage of 5 kV and a probe current of 3 nA. Energy-dispersive X-ray spectroscopy (EDS) was performed using an Oxford Ultim Extreme detector (1024 × 768 pixels) at an acceleration voltage of 3 kV and a current of 3 nA; see also SI Note S6.

Author contributions

Conceptualization: M. H. and R. B.; experimental concept: M. H.; material fabrication: C. S. and S. K.; sample preparation: M. H.; *in situ* measurement: M. H., R. J. S., O. S., J. V. and R. B.; DVC analysis: M. H., R. J. S. and O. S.; visualization: M. H. and R. J. S.; supervision: R. B.; writing: M. H. and R. B. All authors contributed to discussions of the research.

Conflicts of interest

The authors declare no conflicts of interest.

Data availability

All data needed to evaluate the conclusions in the paper are presented in the paper. All underlying nano-SXCT data can be accessed *via* the dataset DOIs: 10.15151/ESRF-ES-1190113340 & 10.15151/ESRF-ES-1579881493. Additional information can be obtained from the corresponding author upon reasonable request.

Code availability: data pre-processing steps and the semantic segmentation model architecture are described in detail in the Materials and methods. The custom code used for data pre-processing, training and analysis is available from the corresponding author upon reasonable request.

© 2026 The Author(s). Published by the Royal Society of Chemistry

Open Access Article. Published on 26 February 2026. Downloaded on 5/23/2026 9:12:27 AM. This article is licensed under a Creative Commons Attribution 3.0 Unported Licence.

Supplementary information (SI) is available. See DOI: https://doi.org/10.1039/d6eb00026f.

Acknowledgements

The authors gratefully acknowledge the financial support by the Austrian Research Promotion Agency (FFG) from the Mobility of the Future programme, Proj. No. 891479 "OpMoSi" and partly under the scope of the COMET program within the K2 Center "Integrated Computational Material, Process and Product Engineering (IC-MPPE)" (Project No 886385) project ASSESS P1.10. This program is supported by the Austrian Federal Ministries for Economy, Energy and Tourism (BMWET) and for Innovation, Mobility and Infrastructure (BMIMI), represented by the Austrian Research Promotion Agency (FFG), and the federal states of Styria, Upper Austria and Tyrol ESRF is acknowledged for beam time allocation and access (proposal MA-4927[80] & MA-6174[81]) at the ID16B beamline. Furthermore, Charlotte Cui is acknowledged for her support during laser preparation.

References

1 X. Wu, G. Ji, J. Wang, G. Zhou and Z. Liang, *Adv. Mater.*, 2023, **35**, 2301540.
2 G. G. Njema, R. B. O. Ouma and J. K. Kibet, *J. Renewable Energy*, 2024, **2024**, 2329261.
3 C. D. Quilty, D. Wu, W. Li, D. C. Bock, L. Wang, L. M. Housel, A. Abraham, K. J. Takeuchi, A. C. Marschilok and E. S. Takeuchi, *Chem. Rev.*, 2023, **123**, 1327–1363.
4 Y.-X. Yao, L. Xu, C. Yan and Q. Zhang, *EES Batteries*, 2025, **1**, 9–22.
5 Y. Zhang, J. C. Kim, H. W. Song and S. Lee, *Nanoscale*, 2023, **15**, 4195–4218.
6 J. Asenbauer, T. Eisenmann, M. Kuenzel, A. Kazzazi, Z. Chen and D. Bresser, *Sustainable Energy Fuels*, 2020, **4**, 5387–5416.
7 G. G. Eshetu, H. Zhang, X. Judez, H. Adenusi, M. Armand, S. Passerini and E. Figgemeier, *Nat. Commun.*, 2021, **12**, 1–14.
8 Z. Zhang, Y. Wu, Z. Mo, X. Lei, X. Xie, X. Xue, H. Qin and H. Jiang, *RSC Adv.*, 2025, **15**, 10731–10753.
9 N. M. Saidi, M. A. A. M. Abdah, M. N. Mustafa, R. Walvekar, M. Khalid and A. Khosla, *Battery Energy*, 2025, e20240048.
10 A. P. Yuda, P. Y. E. Koraag, F. Iskandar, H. S. Wasisto and A. Sumboja, *J. Mater. Chem. A*, 2021, **9**, 18906–18926.
11 M. T. McDowell, S. S. H. Lee, W. D. Nix and Y. Cui, *Adv. Mater.*, 2013, **25**, 4966–4985.
12 T. Vorauer, J. Schöggl, S. G. Sanadhya, M. Poluektov, W. D. Widanage, L. Figiel, S. Schädler, B. Tordoff, B. Fuchsbichler, S. Koller and R. Brunner, *Commun. Mater.*, 2023, **4**, 44.
13 T. Vorauer, P. Kumar, C. L. Berhaut, F. F. Chamasemani, P. H. Jouneau, D. Aradilla, S. Tardif, S. Pouget, B. Fuchsbichler, L. Helfen, S. Atalay, W. D. Widanage, S. Koller, S. Lyonnard and R. Brunner, *Commun. Chem.*, 2020, **3**, 141.
14 L. Y. Beaulieu, K. W. Eberman, R. L. Turner, L. J. Krause and J. R. Dahn, *Electrochem. Solid-State Lett.*, 2001, **4**, A137–A140.
15 D. E. Galvez-Aranda, A. Verma, K. Hankins, J. M. Seminario, P. P. Mukherjee and P. B. Balbuena, *J. Power Sources*, 2019, **419**, 208–218.
16 S. Haufe, R. Bernhard and J. Pfeiffer, *J. Electrochem. Soc.*, 2021, **168**, 080531.
17 D. Jantke, R. Bernhard, E. Hanelt, T. Buhrmester, J. Pfeiffer and S. Haufe, *J. Electrochem. Soc.*, 2019, **166**, A3881–A3885.
18 M. Häusler, O. Stamati, C. Gammer, F. Moitzi, R. J. Sinojiya, J. Villanova, B. Sartory, D. Scheiber, J. Keckes, B. Fuchsbichler, S. Koller and R. Brunner, *Commun. Mater.*, 2024, **5**, 163.
19 M. Je, D.-Y. Han, J. Ryu and S. Park, *Acc. Chem. Res.*, 2023, **56**, 2213–2224.
20 A. Fereydooni, C. Yue and Y. Chao, *Small*, 2024, **20**, 2307275.
21 R. Zhu, Y. Jiang, Y. Song, L. Liu, Y. Xu and H. Pang, *Chem. Eng. J.*, 2024, **490**, 151681.
22 E. Poorshakoor and M. Darab, *J. Energy Storage*, 2024, **75**, 109638.
23 M. N. Obrovac and V. L. Chevrier, *Chem. Rev.*, 2014, **114**(23), 11444–11502.
24 P. Limthongkul, Y.-I. Jang, N. J. Dudney and Y. M. Chiang, *J. Power Sources*, 2003, **119–121**, 604–609.
25 M. Graf, C. Berg, R. Bernhard, S. Haufe, J. Pfeiffer and H. A. Gasteiger, *J. Electrochem. Soc.*, 2022, **169**, 020536.
26 X. H. Liu, L. Zhang, L. Zhong, M. Srezoshnik, S. X. Mao, J. Y. Huang and T. Zhu, *ACS Nano*, 2012, **6**, 1522–1531.
27 Y. He, L. Jiang, T. Chen, Y. Xu, H. Jia, R. Yi, D. Xue, M. Song, A. Genc, C. Bouchet-Marquis, L. Pullan, T. Tessner, J. Yoo, X. Li, J. G. Zhang, S. Zhang and C. Wang, *Nat. Nanotechnol.*, 2021, **16**, 1113–1120.
28 X. H. Liu, J. W. Wang, S. Huang, F. Fan, X. Huang, Y. Liu, S. Krylyuk, J. Yoo, S. A. Dayeh, A. V. Davydov, S. X. Mao, S. T. Picraux, S. Zhang, J. Li, T. Zhu and J. Y. Huang, *Nat. Nanotechnol.*, 2012, **7**, 749–756.
29 Z. Deng, X. Lin, Z. Huang, J. Meng, Y. Zhong, G. Ma, Y. Zhou, Y. Shen, H. Ding and Y. Huang, *Adv. Energy Mater.*, 2021, **11**, 2000806.
30 D. Schäfer, K. Hankins, M. Allion, U. Krewer, F. Karcher, L. Derr, R. Schuster, J. Maibach, S. Mück, D. Kramer, R. Mönig, F. Jeschull, S. Daboss, T. Philipp, G. Neusser, J. Romer, K. Palanisamy, C. Kranz, F. Buchner, R. J. Behm, A. Ahmadian, C. Kübel, I. Mohammad, A. Samoson, R. Witter, B. Smarsly and M. Rohnke, *Adv. Energy Mater.*, 2024, **14**, 2302830.
31 É. A. Santos, M. M. Amaral, B. S. Damasceno, L. M. Da Silva, H. G. Zanin, J. N. Weker and C. B. Rodella, *Nano Energy*, 2024, **130**, 110098.

© 2026 The Author(s). Published by the Royal Society of Chemistry

Open Access Article. Published on 26 February 2026. Downloaded on 5/23/2026 9:12:27 AM. This article is licensed under a Creative Commons Attribution 3.0 Unported Licence.

32 D. L. Nelson, S. E. Sandoval, J. Pyo, D. Bistri, T. A. Thomas, K. A. Cavallaro, J. A. Lewis, A. S. Iyer, P. Shevchenko, C. V. Di Leo and M. T. McDowell, *ACS Energy Lett.*, 2024, **9**, 6085–6095.
33 X. Zhang, M. Osenberg, R. F. Ziesche, Z. Yu, J. Kowal, K. Dong, Y. Lu and I. Manke, *ACS Energy Lett.*, 2025, **10**, 496–525.
34 F. Tariq, V. Yufit, D. S. Eastwood, Y. Merla, M. Biton, B. Wu, Z. Chen, K. Freedman, G. Offer, E. Peled, P. D. Lee, D. Golodnitsky and N. Brandon, *ECS Electrochem. Lett.*, 2014, **3**, A76.
35 D. P. Finegan, M. Scheel, J. B. Robinson, B. Tjaden, I. Hunt, T. J. Mason, J. Millichamp, M. Di Michiel, G. J. Offer, G. Hinds, D. J. L. Brett and P. R. Shearing, *Nat. Commun.*, 2015, **6**, 6924.
36 V. Vanpeene, J. Villanova, A. King, B. Lestriez, E. Maire and L. Roué, *Adv. Energy Mater.*, 2019, **9**, 1803947.
37 V. Vanpeene, J. Villanova, J. P. Suuronen, A. King, A. Bonnin, J. Adrien, E. Maire and L. Roué, *Nano Energy*, 2020, **74**, 104848.
38 V. Vanpeene, L. Huet, J. Villanova, M. Olbinado, F. Marone, E. Maire, L. Roué, T. Devic and B. Lestriez, *Adv. Energy Mater.*, 2025, **15**, 2403741.
39 V. Vanpeene, A. King, E. Maire and L. Roué, *Nano Energy*, 2019, **56**, 799–812.
40 V. Vanpeene, A. Etiemble, A. Bonnin, E. Maire and L. Roué, *J. Power Sources*, 2017, **350**, 18–27.
41 X. Lu, R. E. Owen, W. Du, Z. Zhang, A. Bertei, R. Soni, X. Zhang, F. Iacoviello, D. Li, A. Llewellyn, J. Chen, H. Zhang, X. Yao, Q. Li, Y. Zhao, S. Marathe, C. Rau and P. R. Shearing, *Nat. Nanotechnol.*, 2025, **20**, 1656–1666.
42 G. Martinez-Criado, J. Villanova, R. Tucoulou, D. Salomon, J.-P. Suuronen, S. Labouré, C. Guilloud, V. Valls, R. Barrett, E. Gagliardini, Y. Dabin, R. Baker, S. Bohic, C. Cohen and J. Morse, *J. Synchrotron Radiat.*, 2016, **23**, 344–352.
43 K. Zhang, Y. He, J. Zhou, X. Wang, Y. Li and F. Yang, *RSC Adv.*, 2024, **14**, 29979–29991.
44 C. Tan, S. R. Daemi, O. O. Taiwo, T. M. M. Heenan, D. J. L. Brett and P. R. Shearing, *Materials*, 2018, **11**, 2157.
45 J. Wang, C. Eng, Y. C. K. Chen-Wiegart and J. Wang, *Nat. Commun.*, 2015, **6**, 7496.
46 L. Zielke, C. Barchasz, S. Walu, F. Alloin, J. C. Leprêtre, A. Spettl, V. Schmidt, A. Hilger, I. Manke, J. Banhart, R. Zengerle and S. Thiele, *Sci. Rep.*, 2015, **5**, 1–12.
47 F. Schomburg, B. Heidrich, S. Wennemar, R. Drees, T. Roth, M. Kurrat, H. Heimes, A. Jossen, M. Winter, J. Y. Cheong and F. Röder, *Energy Environ. Sci.*, 2024, **17**, 2686–2733.
48 S. W. Wilkins, T. E. Gureyev, D. Gao, A. Pogany and A. W. Stevenson, *Nature*, 1996, **384**, 335–338.
49 N. A. Chernova, J. B. Cook, R. J. Dashwood and C. P. Grey, *Adv. Mater.*, 2009, **21**, 2767–2770.
50 O. Stamati, E. Andò, E. Roubin, R. Cailletaud, M. Wiebicke, G. Pinzon, C. Couture, R. C. Hurley, R. Caulk, D. Caillerie, T. Matsushima, P. Bésuelle, F. Bertoni, T. Arnaud, A. O. Laborin, R. Rorato, Y. Sun, A. Tengattini, O. Okubadejo, J.-B. Colliat, M. Saadatfar, F. E. Garcia, C. Papazoglou, I. Vego, S. Brisard, J. Dijkstra and G. Birmpilis, *J. Open Source Softw.*, 2020, **5**, 2286.
51 M.-T. F. Rodrigues, A. Y. R. Prado, S. E. Trask, S. Ahmed, A. N. Jansen and D. P. Abraham, *J. Power Sources*, 2020, **477**, 229029.
52 D. Li, H. Wan, H. Liu, Y. Wang and J. Zhang, *Phys. Chem. Chem. Phys.*, 2022, **24**, 25580–25587.
53 E. Feyzi, M. R. Anil Kumar, X. Li, S. Deng, J. Nanda and K. Zaghib, *Next Energy*, 2024, **5**, 100176.
54 K. Fu, X. Li, K. Sun, Z. Zhang, H. Yang, L. Gong, G. Qin, D. Hu, T. Li and P. Tan, *Adv. Funct. Mater.*, 2024, **34**, 2409623.
55 V. A. Sethuraman, M. J. Chon, M. Shimshak, N. Van Winkle and P. R. Guduru, *J. Power Sources*, 2010, **195**, 5062–5066.
56 E. Rejovitzky, C. V. Di Leo and L. Anand, *J. Mech. Phys. Solids*, 2015, **78**, 210–230.
57 O. von Kessel, A. Avdyli, D. Vrankovic and K. P. Birke, *J. Power Sources*, 2024, **610**, 234582.
58 R. De Pascalis, F. Lisi and G. Napoli, *Extreme Mech. Lett.*, 2023, **61**, 102014.
59 C. Chen, T. Zhou, D. L. Danilov, L. Gao, S. Benning, N. Schön, S. Tardif, H. Simons, F. Hausen, T. U. Schülli, R. A. Eichel and P. H. L. Notten, *Nat. Commun.*, 2020, **11**, 3283.
60 A. Wang, S. Kadam, H. Li, S. Shi and Y. Qi, *npj Comput. Mater.*, 2018, **4**, 15.
61 J. Shin, T.-H. Kim, Y. Lee and E. Cho, *Energy Storage Mater.*, 2020, **25**, 764–781.
62 G. Yang, S. Frisco, R. Tao, N. Philip, T. H. Bennett, C. Stetson, J.-G. Zhang, S.-D. Han, G. Teeter, S. P. Harvey, Y. Zhang, G. M. Veith and J. Nanda, *ACS Energy Lett.*, 2021, **6**, 1684–1693.
63 G. M. Veith, M. Doucet, R. L. Sacci, B. Vacaliuc, J. K. Baldwin and J. F. Browning, *Sci. Rep.*, 2017, **7**, 6326.
64 K. S. Chan, W.-W. Liang and C. K. Chan, *J. Phys. Chem. C*, 2019, **123**, 22775–22786.
65 A. Ghaur, C. Peschel, I. Dienwiebel, L. Haneke, L. Du, L. Profanter, A. Gomez-Martin, M. Winter, S. Nowak and T. Placke, *Adv. Energy Mater.*, 2023, **13**, 2203503.
66 P. Heugel, J. Petit, F. Klein and J. Tübke, *Batteries*, 2023, **9**, 449.
67 S. Yoshida, Y. Masuo, D. Shibata, M. Haruta, T. Doi and M. Inaba, *J. Electrochem. Soc.*, 2016, **164**, A6084.
68 H. Valencia, P. Rapp, M. Graf, J. Mayer and H. A. Gasteiger, *J. Electrochem. Soc.*, 2024, **171**, 120507.
69 G. Lu, J. Nai, D. Luan, X. Tao and X. W. Lou, *Sci. Adv.*, 2023, **9**, eadf1550.
70 Y. Li, J. Guo, K. Pedersen, L. Gurevich and D.-I. Stroe, *J. Energy Chem.*, 2023, **80**, 237–246.
71 P. Keil and A. Jossen, *J. Energy Storage*, 2016, **6**, 125–141.
72 M. Häusler, R. Wilhelmer, R. J. Sinojiya, O. Stamati, J. Villanova, C. Stangl, S. Koller and R. Brunner, *J. Mater. Chem. A*, 2025, **13**(36), 29930–29942.

© 2026 The Author(s). Published by the Royal Society of Chemistry

Open Access Article. Published on 26 February 2026. Downloaded on 5/23/2026 9:12:27 AM.
This article is licensed under a Creative Commons Attribution 3.0 Unported Licence.

73 P. Cloetens, W. Ludwig, J. Baruchel, D. Van Dyck, J. Van Landuyt, J. P. Guigay and M. Schlenker, *Appl. Phys. Lett.*, 1999, **75**, 2912–2914.
74 V. Favre-Nicolin, G. Girard, S. Leake, J. Carnis, Y. Chushkin, J. Kieffer, P. Paléo and M.-I. Richard, *J. Appl. Crystallogr.*, 2020, **53**, 1404–1413.
75 P. Paleo, J. Lesaint, H. Payno, A. Mirone, N. Vigano and C. Nemoz, 2024, *Nabu 2024.1, Zenodo*, DOI: 10.5281/zenodo.11104029.
76 O. Ronneberger, P. Fischer, T. Brox, *MICCAI*, 2015, Springer, vol. 9351, 2015, DOI: 10.1007/978-3-319-24574-4_28.
77 S. Berg, D. Kutra, T. Kroeger, C. N. Straehle, B. X. Kausler, C. Haubold, M. Schiegg, J. Ales, T. Beier, M. Rudy, K. Eren, J. I. Cervantes, B. Xu, F. Beuttenmueller, A. Wolny, C. Zhang, U. Koethe, F. A. Hamprecht and A. Kreshuk, *Nat. Methods*, 2019, **16**, 1226–1232.
78 *Dragonfly, 2024.1 [Computer software]*, Comet Technologies Canada Inc., Montreal, Canada; software available at https://dragonfly.comet.tech/, preprint.
79 C. A. Schneider, W. S. Rasband and K. W. Eliceiri, *Nat. Methods*, 2012, **9**, 671–675.
80 M. Häusler, R. Sinojya, O. Stamati, and R. Brunner, [Dataset]. European Synchrotron Radiation Facility, 2023, DOI: 10.15151/ESRF-ES-1190113340.
81 M. Häusler, R. Sinojya, O. Stamati, and R. Brunner, [Dataset]. European Synchrotron Radiation Facility, 2024, DOI: 10.15151/ESRF-ES-1579881493.

© 2026 The Author(s). Published by the Royal Society of Chemistry